Atmos. Chem. Phys., 14, 7045–7057, 2014
www.atmos-chem-phys.net/14/7045/2014/
doi:10.5194/acp-14-7045-2014

Atmospheric Chemistry and Physics
Open Access

Dispersion of the Nabro volcanic plume and its relation to the Asian summer monsoon

T. D. Fairlie[1], J.-P. Vernier[2], M. Natarajan[1], and K. M. Bedka[2]

[1]NASA Langley Research Center, Hampton, Virginia 23681, USA
[2]Science Systems and Applications, Inc., Hampton, Virginia 23666, USA

Correspondence to: T. D. Fairlie (t.d.fairlie@nasa.gov)

Received: 30 August 2013 – Published in Atmos. Chem. Phys. Discuss.: 19 December 2013
Revised: 21 March 2014 – Accepted: 20 May 2014 – Published: 10 July 2014

Abstract. We use nighttime measurements from the Cloud Aerosol Lidar and Infrared Pathfinder Satellite Observation (CALIPSO) satellite, together with a Lagrangian trajectory model, to study the initial dispersion of volcanic aerosol from the eruption of Mt. Nabro (Ethiopia/Eritrea) in June 2011. The Nabro eruption reached the upper troposphere and lower stratosphere (UTLS) directly, and the plume was initially entrained by the flow surrounding the Asian anticyclone, which prevails in the UTLS from the Mediterranean Sea to East Asia during boreal summer. CALIPSO detected aerosol layers, with optical properties consistent with sulfate, in the lower stratosphere above the monsoon convective region in South and Southeast Asia within 10 days of the eruption. We show that quasi-isentropic differential advection in the vertically sheared flow surrounding the Asian anticyclone explains many of these stratospheric aerosol layers. We use Meteosat-7 data to examine the possible role of deep convection in the Asian monsoon in transporting volcanic material to the lower stratosphere during this time, but find no evidence that convection played a direct role, in contrast with claims made in earlier studies. On longer timescales, we use CALIPSO data to illustrate diabatic ascent of the Nabro aerosol in the lower stratosphere at rates of ∼ 10 K per month for the first two months after the eruption, falling to ∼ 3 K per month after the Asian anticyclone dissipates. Maps of stratospheric aerosol optical depth (AOD) show local peaks of ∼ 0.04–0.06 in July in the region of the Asian anticyclone; we find associated estimates of radiative forcing small, ∼ 5–10 % of those reported for the eruption of Mt. Pinatubo in 1991. Additionally, we find no clear response in outgoing shortwave (SW) flux due to the presence of Nabro aerosol viewed in the context of SW flux variability as measured by CERES (Clouds and Earth Radiant Energy System).

1 Introduction

Injections of SO_2 into the stratosphere from large volcanic eruptions can lead to sulfate aerosols that persist for months–years, with a significant impact on Earth's radiative budget (McCormick et al., 1995; Robock et al., 2000) and on chemical processes in the low stratosphere (Rodriguez et al., 1991; Solomon et al., 1993; Portman et al., 1996). The powerful eruption of Mt. Pinatubo in June 1991, for example, injected ∼ 20 Tg of SO_2 into the atmosphere (Bluth et al., 1992; Guo et al., 2004); the resultant sulfate cloud persisted for several years and reduced the global mean surface temperature by up to ∼ 0.5 °C in the following year (McCormick et al., 1995). After a relatively quiescent period of 10 years following the Mt. Pinatubo eruption, the stratospheric background aerosol loading reached a minimum, but in the past decade small but frequent eruptions have led to increased stratospheric aerosol levels (Vernier et al., 2011a, Neely et al., 2013), which may have mitigated warming by greenhouse gases by up to 25 % (Solomon et al., 2011).

The major eruption of Mt. Nabro, a 2218 m high volcano on the border between Eritrea and Ethiopia (13.37° N, 41.7° E), on 12–13 June, 2011, is considered the largest single injection of SO_2 to the stratosphere since the eruption of Mt. Pinatubo (Krotkov et al., 2011). Ash, water vapor, and an estimated 1.3–2.0 Tg of SO_2 were injected into the upper troposphere and lower stratosphere (UTLS) (Krotkov et al., 2011; Clarisse et al., 2012; Sawamura et al., 2012). The

volcanic plume was initially entrained by the flow surrounding the Asian anticyclone circulation, which prevails from the Mediterranean Sea to East Asia in the UTLS during boreal summer, as shown by SO_2 and aerosol measurements from the Ozone Monitoring Instrument (OMI) (Krotkov et al., 2011), the InfraRed Atmospheric Sounding Instrument (IASI) (Clarisse et al., 2012), the Microwave Limb Sounder (MLS) (Fromm et al., 2013), and CALIPSO (Cloud Aerosol Lidar and Infrared Pathfinder Satellite Observation; Vernier et al., 2013a). From early July, however, detrainment pathways across the northern Pacific and the tropical Atlantic led to dispersal of aerosol in the lower stratosphere throughout the Northern Hemisphere, as evidenced by observations from the Optical Spectrograph and Infrared Imaging System (OSIRIS) (Bourassa et al., 2012), from CALIPSO, and from global networks of ground-based lidar systems (Sawamura et al., 2012).

While it is well known that explosive volcanic eruptions can inject materials directly into the stratosphere and affect climate, Bourassa et al. (2012) proposed a new mechanism by which less intense eruptions can reach stratospheric altitudes. They indicated that in the case of the Nabro eruption the plume was injected exclusively into the troposphere (9–13 km), and "only reached stratospheric altitudes through subsequent transport processes associated with deep convection," within the summer Asian monsoon. If true, deep convection in the monsoon would provide an important alternative vehicle for rapid transport of volcanic sulfate to the stratosphere. Bourassa et al. (2012) concluded that "volcanic eruptions need not reach the stratosphere directly to affect climate." However, Vernier et al. (2013a) and Fromm et al. (2013) showed that the Nabro eruption penetrated the cold-point tropopause directly, and showed volcanic material in the low stratosphere well before encountering deep convection associated with the Asian monsoon. Here, we present additional evidence to explain the appearance of volcanic layers in the low stratosphere above the monsoon region in the first 2 weeks following the eruption. We also use the CALIPSO observations to infer net mean diabatic ascent rates in the lower stratosphere in the Asian region over longer (months) timescales, and use radiative transfer calculations to estimate the contribution of the aerosol layer to TOA (top-of-the-atmosphere) radiative forcing.

We use nighttime level-1 aerosol backscatter observations from the CALIPSO satellite, and a Lagrangian trajectory model, to characterize the initial three-dimensional (3-D) dispersion of the volcanic plume, and to interpret observations made from ground-based sites. CALIPSO has provided an unprecedented 3-D view of aerosol and cloud layers in the atmosphere since 2006 (Winker et al., 2010), and has been used to accurately estimate the altitude and vertical layering of volcanic plumes (Vernier et al., 2009). Recently, cloud-cleared scattering-ratio (SR) data from CALIPSO have been combined with trajectory calculations to monitor diffuse volcanic ash for aircraft safety (Vernier et al., 2013b). In this paper, we identify the Nabro volcanic plume when the 532 nm volume depolarization ratio is below 5 % following Vernier et al. (2009). This criterion mainly isolates volcanic sulfate layers from ice clouds but also filters ash, which we have determined to be only a minor component of the Nabro plume in the UTLS (see Fig. S1 in the Supplement, and accompanying discussion).

We use trajectory calculations in two distinct ways: first, we present a simple "source" simulation of the initial dispersion; results are compared with ground-based and CALIOP lidar observations downstream; second, we use trajectory calculations to map cloud-cleared CALIPSO SR observations to synoptic times coincident with brightness temperature maps from Meteosat-7, to assess the potential role of deep convection, associated with prominent mesoscale convective systems (MCSs), in the monsoon region, in transporting sulfate to the stratosphere.

The plan of the paper is as follows: in Sect. 2, we provide meteorological context for the Nabro eruption, and present the trajectory calculations used to simulate the plume's initial dispersion. We compare the results with ground-based MPLNET (Micropulse Lidar Network) lidar observations from Sede Boker, Israel, 1–2 days after the eruption, and with CALIOP lidar observations downstream. We show isentropic analyses and cross sections of the simulated and observed aerosol plumes along CALIPSO orbit tracks for the 10 days following the eruption. In Sect. 3, we examine likely coincidences of the Nabro material in the upper troposphere with MCSs, using Meteosat-7 brightness temperatures as a proxy for convective activity. We use trajectory mapping of volcanic layers subsequently observed by CALIPSO in the low stratosphere to assess the case that deep convection may explain those observations. In Sect. 4, we use cloud-cleared CALIPSO SR data to examine the longer-term ascent of volcanic aerosol in the stratosphere over the 6 months following the eruption, and estimate the resultant aerosol optical depth, and associated TOA radiative forcing.

2 Initial dispersion of the Nabro volcanic plume in the UTLS

2.1 Atmospheric environment for the volcanic eruption

Figure 1 shows maps of wind speed and diabatic heating rate on the 380 K surface of potential temperature, θ, at 00:00 Z (Zulu time), 13 June 2011, taken from GEOS-5.2 meteorological analyses (Rienecker et al., 2008). Also shown are cross sections of these quantities at 40° E for the same date and time. The maps and cross sections provide a snapshot of the meteorological context in which the Nabro volcano erupted. Here and hereafter, we follow Holton et al. (1995), and Schoeberl (2004) in using the $\theta = 380$ K isopleth to delineate an upper bound to the tropical tropopause, recognizing that air masses with mixed tropospheric and stratospheric

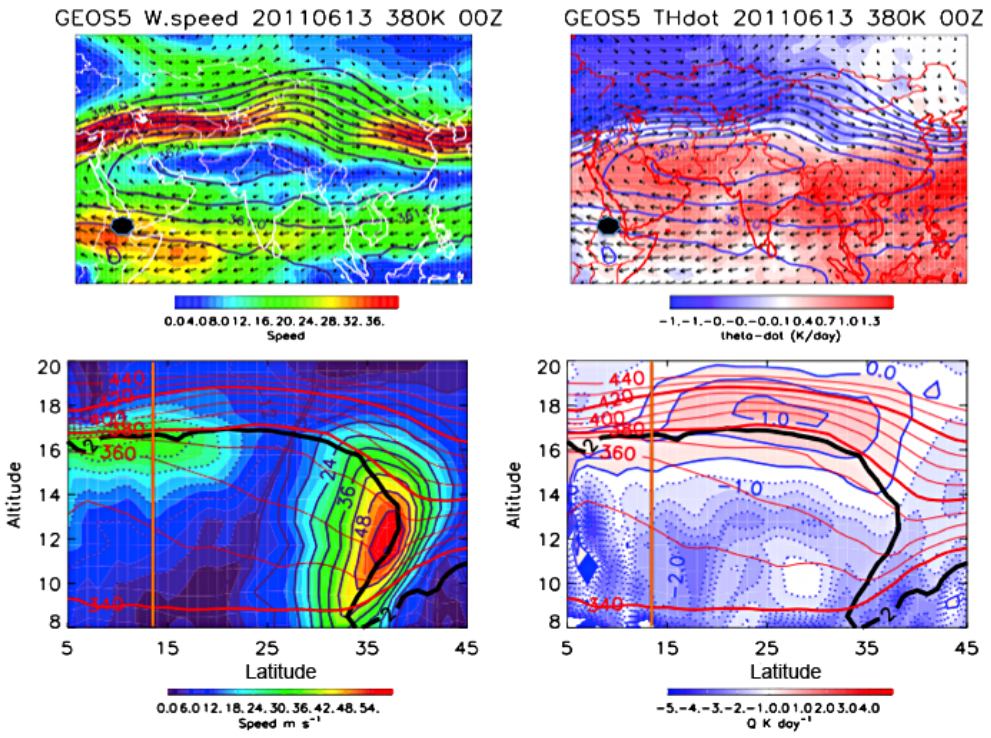

Figure 1. Top: maps of wind speed and diabatic heating rate at 380 K potential temperature, θ, for 00:00 Z, 13 June 2011. Isopleths of MSF, and wind vectors are also shown. A black spot marks the location of Mt. Nabro. Bottom: cross sections of wind speed and diabatic heating rate at 40° E for the same date and time. Isopleths of θ, PV = 2.0 PVU, and vectors of the meridional wind component are also shown, an orange vertical line marks the latitude of Mt. Nabro. The resolution of the GEOS-5.2 data shown is 1.25° × 1° in the horizontal, ∼ 1 km in the vertical for the altitudes shown.

properties can be found in a layer (the tropical tropopause layer, or TTL) a few kilometers above and below this level (Fueglistaler et al., 2009). The 380 K surface describes the level above which air parcels must experience diabatic cooling to reach the troposphere (Holton et al., 1995). In the extratropics, the tropopause is more appropriately delineated by an isopleth of potential vorticity (PV) - here we use the PV = 2.0 PVU (PV units) isopleth. Comparatively rapid exchange between the extratropical lowermost stratosphere (θ < 380 K) and tropical upper troposphere helps sustain the mixed TTL (Randel and Jensen, 2013).

Contours of Montgomery stream function (MSF), and wind vectors in Fig. 1, delineate the Asian anticyclone circulation, which extends from the eastern Mediterranean to the western Pacific, flanked to the north by the subtropical jet, and to the south by tropical easterlies. The cross section at 40° E shows the tropical tropopause (380 K) at ∼ 17 km (∼ 100 hPa), just above the PV = 2.0 isopleth. North of the subtropical jet at ∼ 35° N, the PV = 2.0 and 380 K isopleths diverge; confluence in strong west–southwesterly flow leads to marked folding of the extratropical tropopause to ∼ 8 km (∼ 350 hPa) on the northern flank of the jet. The figure indicates that volcanic material injected into the UTLS from Mt. Nabro was subject initially to east–southeasterly flow of up to 40 m s^{-1}, with peak winds just below 17 km.

Vernier et al. (2013a) showed cloud-top brightness temperatures (BTs) from the SEVIRI (Spinning Enhanced Visible and Infrared Imager) instrument on Meteosat-9 immediately following the eruption (their Fig. 3), illustrating the anvil of the volcanic plume spreading northwestward from the volcano. The anvil featured a BT of ∼ 192 K, together with an area of enhanced BT of ∼ 203 K directly above the volcano, the latter characteristic of penetration of the cold-point tropopause. The closest radiosonde profile (Abha airport, Saudi Arabia, not shown) indicates that the anvil lay at ∼ 80 hPa, (altitude ∼ 18 km, θ ∼ 390 K), while the 203 K hotspot penetrated as high as ∼ 75 hPa, (altitude ∼ 19 km, θ ∼ 425 K), in the low stratosphere. In response to Vernier et al. (2013a) and Fromm et al. (2013), Bourassa et al. (2013) noted the coldest point in the Abha profile at ∼ 78 hPa (θ ∼ 396 K), maintaining their argument for a purely tropospheric injection. While there is little doubt that much of the erupted material was injected into the upper troposphere, material found above 380 K was subject to the stratified flow conditions characteristic of the stratosphere (see above).

Figure 1 also indicates the level of zero diabatic heating (LZDH) at ∼ 15 km, with volcanic material injected

above this level subject to net diabatic heating of up to $\sim 0.5\,\mathrm{K\,day^{-1}}$. Lower altitudes are subject to net cooling. Elsewhere in the Asian anticyclone, particularly in the south and east, net diabatic heating reaches 1–1.5 $\mathrm{K\,day^{-1}}$ between 380 and 420 K.

2.2 Simulated dispersion and comparison with lidar observations at Sede Boker, Israel

We use the NASA Langley trajectory model (LaTM; Pierce et al., 1994, 1997; Fairlie et al., 2009) to study the initial dispersion of the Nabro plume in the UTLS, and to map cloud-cleared CALIPSO SR data to deep convective complexes observed from geostationary satellites (Sect. 3). The LaTM uses a 15 min, fourth-order Runge–Kutta time step to compute 3-D kinematic trajectories, and is driven by the NASA Global Modeling and Assimilation Office (GMAO) GEOS 5.2-analyzed winds (Rienecker et al., 2008). Here, we use 6-hourly, time-averaged wind fields, resolved to $1.25^\circ \times 1^\circ$ in the horizontal, with 72 levels in the vertical at a resolution of ~ 1 km near the tropopause. At each time step, 3-D winds are interpolated linearly in space and time to parcel positions. Three-dimensional trajectories computed using dynamically consistent analysis wind fields are considered the most accurate (Stohl et al., 1998). Nevertheless, we do not rely on the accuracy or representativeness of individual trajectories, but initialize clusters of parcels that permit dispersion due to horizontal and vertical wind shears, recognizing the chaotic nature of synoptic-scale atmospheric flows (Pierce and Fairlie, 1993). We do not represent subgrid-scale convective or turbulent dispersion.

To study the initial dispersion of the Nabro eruption plume, we released air parcels in two concentric circles with radii of 10 and 20 km from the Nabro volcano, spanning altitudes of 12–19 km, at 50 m intervals in the vertical. We included a column of points at the center. Parcels were released every 15 min for 4 h, beginning at 18:00 Z, 12 June 2011, based upon satellite observations of the eruption from SEVIRI. With 8 parcels in each ring, at completion of the 4 h initialization, (2 rings $\times$ 8 parcels per ring $+1$ center point) $\times$ 141 levels $\times$ 16 time steps yields a total of 38 352 parcels released in the model, and their trajectories computed. Less intense eruptions on subsequent days are not represented. In what follows, we restrict our analysis to those parcels initialized at $\theta = 420$ K (~ 18.5 km) and below.

The initial dispersion of the Nabro plume is illustrated in Fig. 2, which shows a map of SO_2 index from AIRS/Aqua observations (Carn et al., 2005) on 14 June, and a map of simulated air parcels for the same day. Also shown in Fig. 2 is a time–height curtain of normalized backscatter from the MPLNET site in Sede Boker, Israel (30.9° N, 34.8° E), on 14 June, comprising the earliest ground-based observations of the volcanic plume (Sawamura et al., 2012), and a corresponding curtain from the trajectory simulation. Also shown are latitude cross sections at 35° E, showing the location of the air parcels for the period 00:00–12:00 Z and 12:00–23:00 Z, 14 June, with respect to the wind, and θ fields, and the PV = 2 isopleth.

AIRS shows the entrainment of the SO_2 plume in strong southwesterly flow over the Middle East on the northwest flank of the Asian anticyclone. The MPLNET lidar at Sede Boker was well positioned to sample the volcanic plume; the head of the plume was first detected at $\sim$ 04:00 Z on 14 June, between 15 and 16 km altitudes. Later in the day, separate upper- and lower-level plume "tails" were observed, consistent with differential advection, due to vertical shear in the strong southwesterly flow. "Stalactite" features in the upper layer (Fig. 2c) suggest possible gravitational settling of the larger particles.

The simulation captures the entrainment of the plume into the southwesterly flow, and shows a similar vertical structure to that observed in passing over Sede Boker. The head of the simulated plume arrives at $\sim$ 04:00 Z, at an altitude of ~ 15 km, with trailing layers at higher and lower altitudes. The timing of its arrival and BT of the erupting plume (Vernier et al., 2013a) supports the release period and vertical range used in the simulation. The fast-moving head of the simulated plume comprises parcels initialized in the upper troposphere, between $\theta = 355$ and 375 K, which (at $\sim 31^\circ$ N) span the tropopause (PV = 2 PVU). Later in the day, air parcels initialized in the lower stratosphere, ~ 380 K and above, and at lower altitudes (~ 13 km) arrive. Later, we show that the slower moving parcels initialized above 380 K account for the stratospheric aerosol layers observed by CALIPSO in South and East Asia in the week to 10 days following the eruption.

The observed plume at Sede Boker is $\sim$ 500–800 m higher in altitude (and up to 10 K in θ) than in the simulation, suggesting that more of the actual plume lies in the lowermost stratosphere than is simulated. However, this altitude discrepancy is within the ~ 1 km vertical resolution of the meteorological data used in the simulation at these altitudes. An alternative explanation for this discrepancy is self-lofting of the volcanic plume through radiative absorption. Background radiative heating in the GEOS-5 fields peaks at $\sim 1\,\mathrm{K\,day^{-1}}$ between 15 and 20 km (Fig. 1). We used the NASA Langley Fu-Liou radiative transfer code (Rose et al., 2006; Natarajan et al., 2012) to estimate of the radiative heating contribution of the Nabro aerosol layer, based on an extinction profile for the volcanic plume observed by CALIPSO on 15 June at 43° N, 50° E (Fig. 1 of Vernier et al., 2013a); the code computes clear-sky radiative-flux profiles with and without aerosols from which the heating rate due to the aerosols can be derived. To estimate extinction we assumed a lidar ratio of 50 sr, consistent with aged sulfate (Müller et al., 2007), and with Raman lidar measurements of the plume reported by Sawamura et al. (2012). We found peak aerosol heating rates of $\sim 0.3\,\mathrm{K\,day^{-1}}$ between 16 and 17 km altitude. (Assuming a higher lidar ratio of 70 sr raised the peak heating only to $\sim 0.4\,\mathrm{K\,day^{-1}}$). Heating rates of $3\,\mathrm{K\,day^{-1}}$ or more

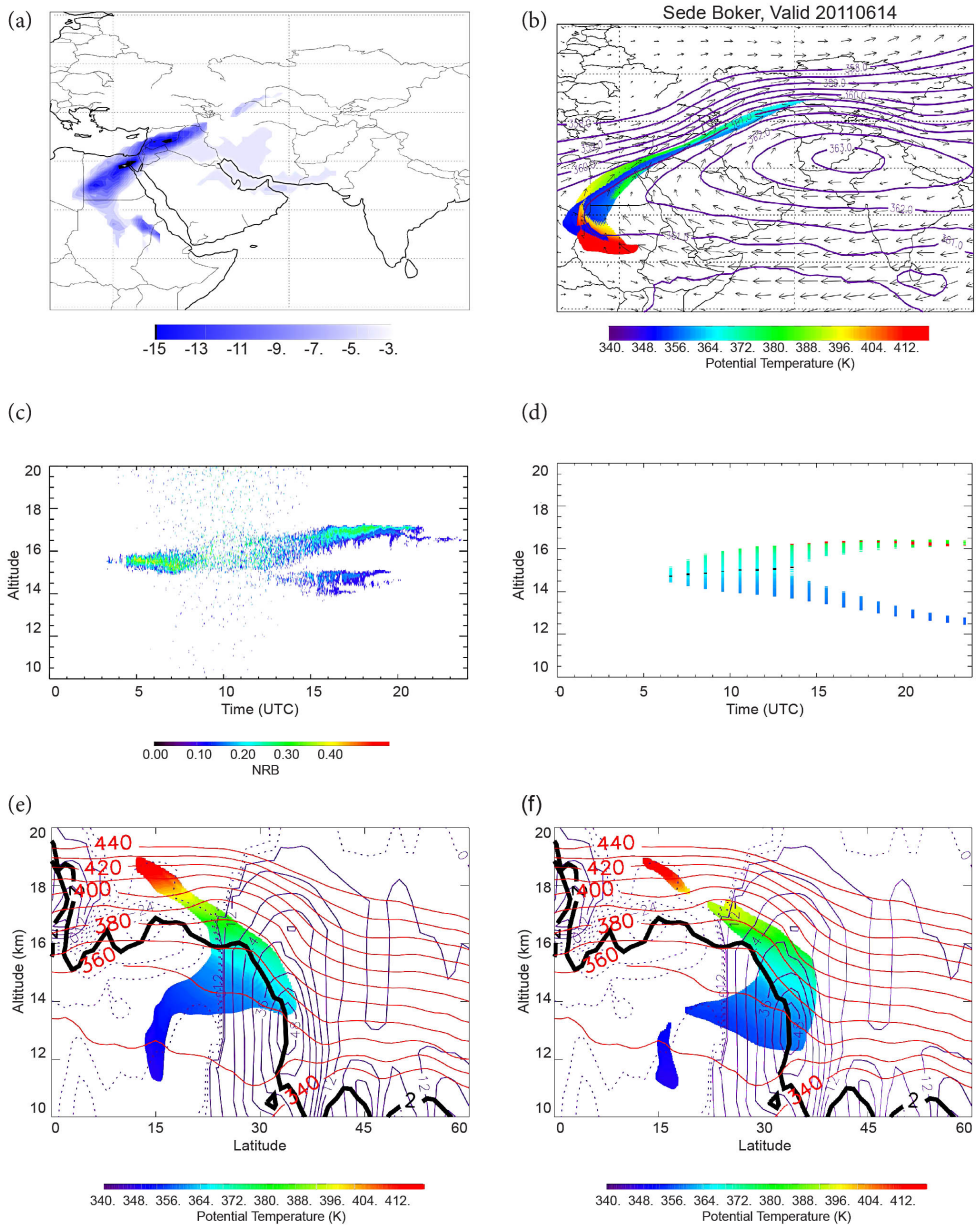

Figure 2. Maps of **(a)** SO_2 index, based on BT differences assembled from AIRS/Aqua, for 14 June 2011, and **(b)** simulated air parcel locations for the same day; **(c)** time–height curtain of normalized backscatter from the MPLNET site at Sede Boker, Israel, on 14 June, and **(d)** corresponding curtain of trajectory locations. MPLNET data provided courtesy of A. Karnieli, B. Gurion University, Israel, and E. J. Welton, NASA GSFC. The air parcel trajectories are colored by their initial θ values, except for those for which PV = 2.0 PVU (red), or θ = 380 K (black); **(e)** and **(f)** cross sections of AM (left) and PM (right) air parcel locations at 35° E on 14 June, colored by initial θ together with 12:00 Z wind speed, θ, and PV = 2 PVU isopleth.

are needed to explain the θ discrepancy, further suggesting that limited vertical resolution of the meteorological analyses is a more likely explanation.

We note in passing that the simulated transport is sensitive to marked vertical wind shear near Mt. Nabro, which may not be adequately captured given the limits of resolution in meteorological analyses. Trajectory calculations shown by Bourassa et al. (2013, their Fig. 2a) and by Sawamura et al. (2012, their Fig. 2) use the same trajectory model (HYSPLIT) but show different results – specifically an altitude difference of ∼ 2 km above which trajectories track west from the volcano, rather than being entrained into the Asian anticyclone. Our results, obtained with GEOS-5.2 analyses, appear consistent with those of Sawamura et al. (2012), who used GDAS (Global Data Assimilation System) meteorological data, and with those of M. von Hobe et al. (personal

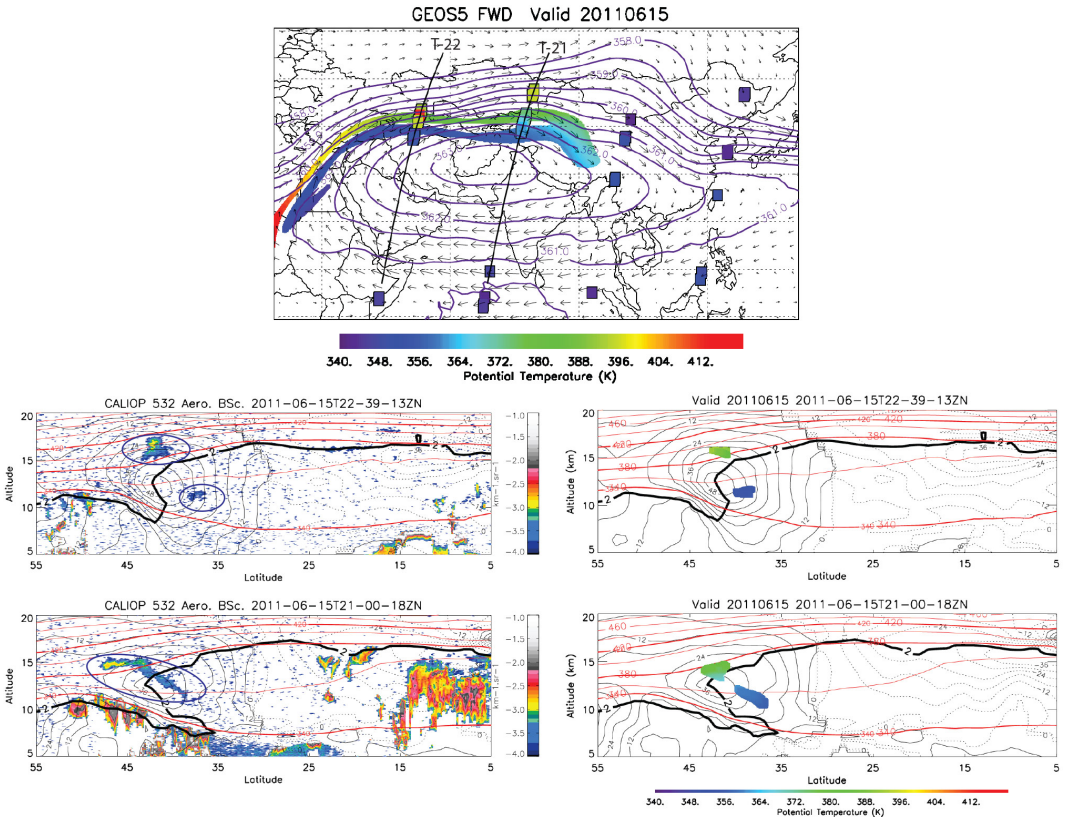

Figure 3. Top: map of air parcel locations from 18:00 Z to midnight on 15 June, from the trajectory source simulation (colored by initial θ), and cloud-cleared level-2 CALIPSO aerosol tops (squares, colored by θ). Contours of MSF (purple) and wind vectors at 380 K are also shown. Left: 532 nm attenuated aerosol backscatter curtains. Right: coincident trajectory curtains for the CALIPSO nighttime orbits crossing the plumes T22-39-13ZN and T21-00-18ZN , and marked by black curves on the map (top). Trajectories within 5° of longitude are projected on to the cross sections. Nabro aerosol layers are highlighted by ovals. Isopleths of wind speed (signed by zonal wind component) (thin, black), θ (red), and PV = 2.0 PVU (bold, black) are also shown.

communication, 2013), who have used ECMWF (European Centre for Medium-Range Weather Forecasts) ERA-interim reanalyses (http://apps.ecmwf.int/datasets/data/interim_full_daily/).

Recirculation of the Nabro plume in the Asian anticyclone resulted in a return of the Nabro plume over Sede Boker on 23 June (Sawamura et al., 2012). Our Lagrangian source simulation shows the first return of Nabro aerosol between 14 and 16 km on that day, consistent with the MPLNET lidar observations (not shown).

2.3 Comparison with CALIOP observations of the Nabro plume

Figure 3 shows a map of air parcel trajectories, colored by initial θ, for 18:00 Z–midnight on 15 June. Superimposed on the map are cloud-cleared level 2 aerosol tops along CALIPSO orbital tracks (squares colored by θ). Contours of MSF and wind vectors at 380 K are also provided. Figure 3 also shows curtains of 532 nm CALIPSO attenuated aerosol backscatter (total minus molecular backscatter), and coincident trajectory curtains for orbits that cross the plume at ∼ 52 and ∼ 78° E (T22-39-13ZN and T21-00-18ZN, respectively). Wind-speed and θ isopleths, and the PV = 2 contour, provide meteorological context to the curtains. The volcanic aerosol appears as moderate aerosol backscatter features ($\log_{10}$ exponents $< \sim -3$) at ∼ 43° N, 390–410 K, above the jet core in the lower stratosphere, at 37° N, 350 K, south of the jet core in the upper troposphere (T22-39-13ZN curtain), and as a filament extending from ∼ 48° N, 390 K in the lower stratosphere to 40° N, 360 K in the upper troposphere (T21-00-18ZN curtain). These features are characterized by low depolarization (< 5 %) characteristic of sulfate aerosol (not shown). Backscatter $\log_{10}$ exponents $> \sim -2.7$ show clouds. Cross sections through the simulated plume show features that closely match those in the CALIPSO curtains, particularly for the western curtain (T22-39-13ZN). At the same time, CALIPSO shows stratospheric components of the plume at a somewhat higher θ (400–420 K) than is simulated for the west curtain, and dispersed farther north at ∼ 400 K in the east curtain (T21-00-18ZN).

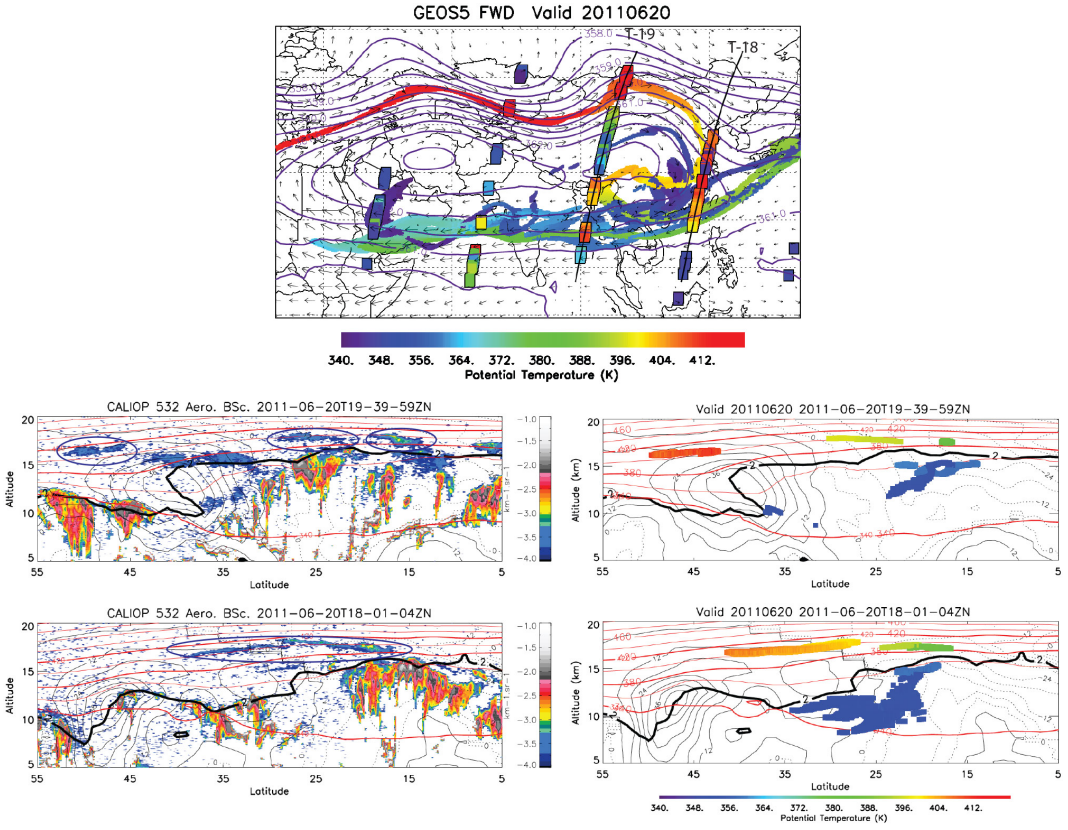

Figure 4. As for Fig. 3, but for 18:00 Z–midnight on 20 June with 532 nm attenuated aerosol backscatter curtains, and coincident trajectory curtains for CALIPSO nighttime orbits T19-39-59ZN and T18-01-04ZN, marked by black curves on map (top).

Figure 3, together with Fig. 2, paints a clear picture of a fast-moving head of the plume between ∼360 and 380 K, transported on the inside (south side) of the jet core, followed by trailing plume tails at higher and lower potential temperatures in the lower stratosphere and upper troposphere, respectively. We have examined BTs from Meteosat-7 for this period and have found no evidence that the volcanic plume encountered deep convection up to this time. Indeed, the T21-00-18ZN curtain, which crosses the plume at ∼78° E, shows how ice clouds are effectively capped at ∼11 km (below the jet core) by enhanced static stability associated with the depressed, extratropical tropopause.

Figures 4 and 5 show corresponding maps and orbital cross sections from 18:00 Z to midnight on 20 and 22 June 2011, as the head of the plume completes one circuit of the Asian anticyclone. We highlight this period because it coincides with the first appearance of aerosol tops at ∼400–420 K in the low stratosphere over South and Southeast Asia. These features appear as thin filaments of moderate aerosol backscatter, above an elevated tropical tropopause in the CALIPSO curtains in Figs. 4 and 5. Bourassa et al. (2013) claimed that coincident high SO_2 in MLS observations in this region provided "convincing evidence for convective lofting of the volcanic plume." However, cross sections through the simulated plume in Figs. 4 and 5 show that much of the observed stratospheric aerosol layering is well represented by air parcels initialized between 380 and 420 K (green–red) above the volcano, and transported quasi-isentropically in vertically sheared flow; the material arrives days after the head of the plume which was advected closer to the jet core. Although it is tempting to use the proximity of the stratospheric layers of volcanic aerosol in the CALIPSO curtains and the ice clouds capped ∼1–2 km below to infer a connection, we find no such connection is needed nor justified to account for the observations.

Not all of the observed aerosol features in CALIPSO curtains are reproduced in the simulation; nor are all features in the simulation vindicated by observations. The aerosol feature at ∼30–40° N, 380 K in curtain T19-39-59ZN (Fig. 4), for example, is barely represented in the simulation (the altitude and location are consistent with material injected subsequent to the main eruption, which we do not simulate here). Simulated aerosol at ∼10–12 km at ∼25–35° N in T18-01-04 (Fig. 4) is absent in the CALIPSO curtain (lack of scavenging in the simulation may be responsible); simulated aerosol between ∼15 and 25° N in the troposphere in curtain T19-27-35ZN (Fig. 5) does not appear in the CALIPSO curtain (attenuation by cloud, scavenging, or both, may be

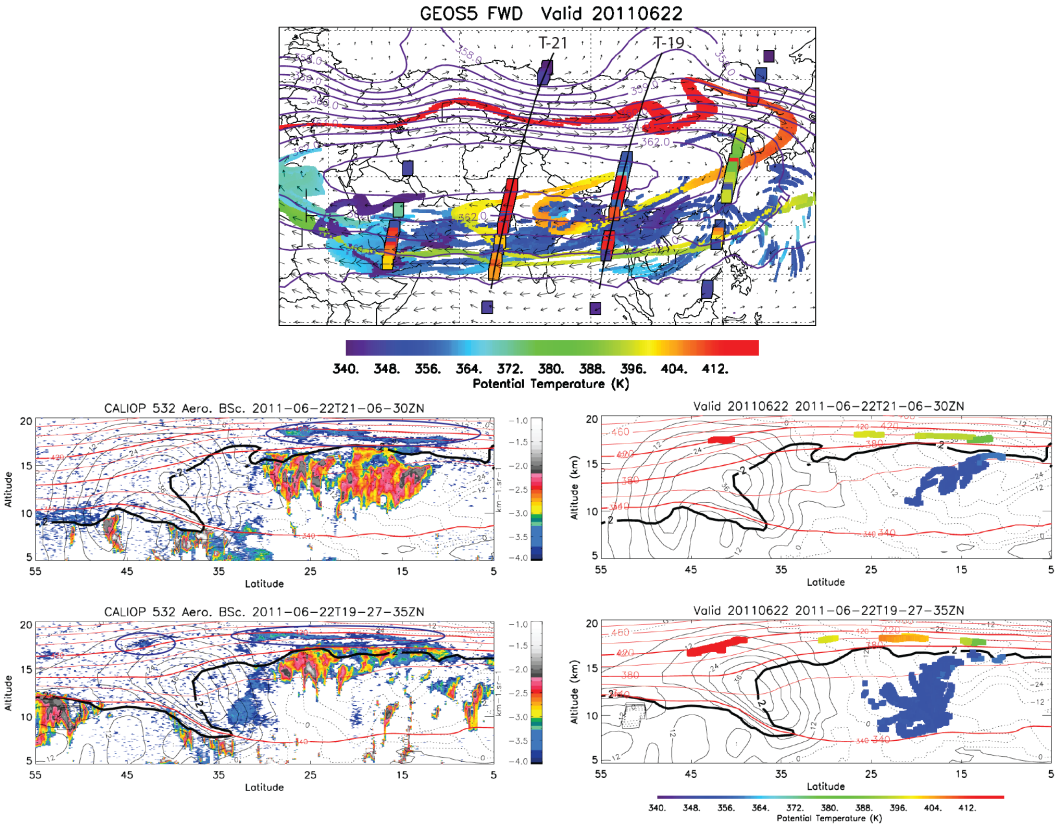

Figure 5. As for Fig. 3, but for 18:00 Z–midnight on 22 June, with 532 nm attenuated aerosol backscatter curtains, and coincident trajectory curtains for CALIPSO nighttime orbits T21-06-30ZN and T19-27-35ZN, marked by back curves on map.

responsible). We do not expect our simple kinematic dispersion simulation to fully reproduce observations, especially those in the troposphere, where the resolved winds represent less of the overall mass transport and wet scavenging is a likely loss mechanism. Our purpose here is to show, very simply, that much of the observed stratospheric aerosol layering in South and Southeast Asia in the week to 10 days following the eruption can be explained by direct stratospheric injection, followed by quasi-isentropic advection, rather than by invoking more complex (e.g., deep convective) mechanisms.

3 Possible interaction of the Nabro plume with mesoscale convective complexes

In this section, we use a combination of satellite BT imagery from Meteosat-7, and the source simulation described in Sect. 2, to identify likely coincidences of deep convection with tropospheric parts of the Nabro plume. We then use forward and backward trajectories initialized with CALIOP observations of the plume, to further assess the case for deep convective transport of Nabro material into the lower stratosphere, as claimed by Bourassa et al. (2012, 2013). Figure 6 (top) shows 10.8 µm BT images from Meteosat-7 on 17 June at 00:00 and 18:00 Z. Air parcel trajectories from the source simulation, colored by their potential temperatures, are superimposed. We focus on two prominent mesoscale convective systems (MCS), highlighted by red boxes in the satellite imagery, because they coincide with leading parts of the simulated volcanic plume near 360–370 K in the upper troposphere. These MCSs exhibit BTs near 190 K, indicating that they reach levels near the tropopause, and represent candidate vehicles for moist convective transport of volcanic material to higher altitudes.

To assess if stratospheric aerosol layers observed subsequently by CALIOP can be traced back to these MCS, we computed back trajectories from elevated aerosol (SR > 1.3) encountered at or above 400 K between 17 and 22 June. The CALIPSO data were sampled at 1° intervals in latitude and 200 m in the vertical along the orbital tracks. We tagged the air parcel trajectories with their original SR values, and accumulated these tagged trajectories as the back-trajectory simulation proceeded and more CALIOP observations were encountered. Figures 4 and 5 (above) have shown that the stratospheric aerosol layers were well sampled by CALIOP in the southern and eastern parts of the Asian anticyclone, downstream of these MCSs, during this period. Figure 6

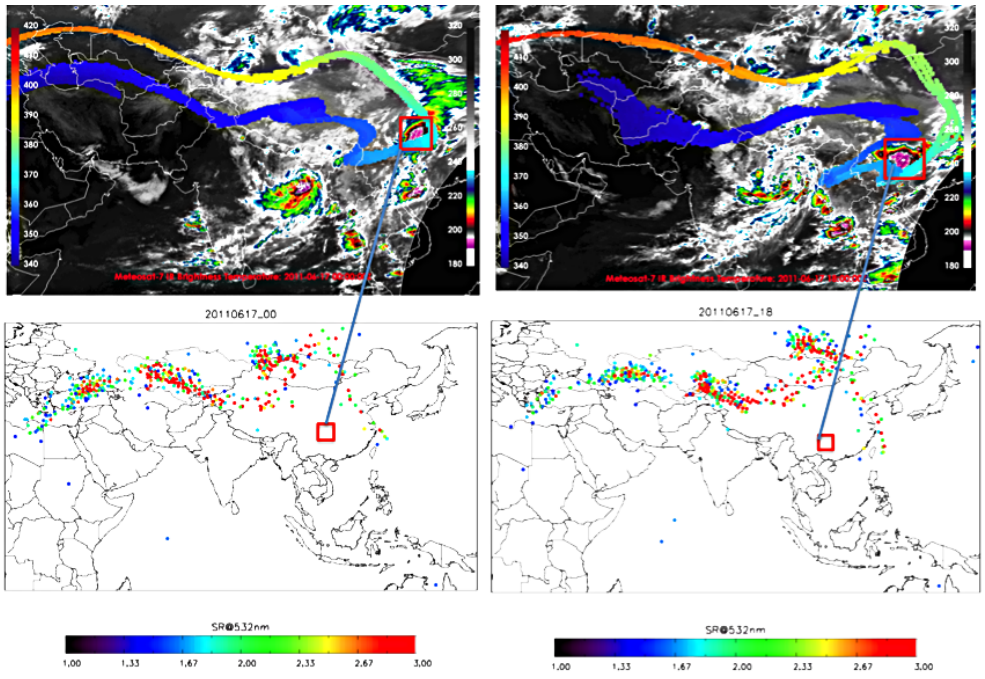

Figure 6. Top panels: 10.8 m cloud-top brightness temperatures (BTs) from Meteosat-7 for 17 June 2011 at 00:00 and 18:00 Z, with air parcel trajectories, colored by θ, from the source simulation, superimposed. Red squares mark the location of MCSs, with BTs of $\sim$ 190 K. Bottom panels: maps of air parcels observed by CALIOP between 17 and 22 June, with $\theta > 400$ K, and SR > 1.3, which have been trajectory-mapped to coincide with the Meteosat-7 maps (top). Trajectories colored (tagged) by associated SR.

shows the resultant trajectory-mapped analyses for 17 June, coincident with the Meteosat-7 images. If the stratospheric aerosol layers, shown in Figs. 4 and 5, were associated with the highlighted MCSs, we would expect to see spatial and temporal coincidence between the MCSs and the trajectory-mapped air parcels. Instead, we find that the back trajectories end up well upstream of the MCSs. Furthermore, we computed forward trajectories for air parcels initialized between 17 and 19 km above the MCSs on 17 June (not shown). These indicate that if the MCSs had lofted Nabro aerosol into the low stratosphere CALIPSO would have detected aerosol layers much further west than was the case, e.g., along the orbit (T22-57-44ZN) track which crosses the Arabian Peninsula on 20 June (Fig. 4). We conclude that these particular MCSs did not play a significant role in transporting Nabro aerosol to the lower stratosphere.

4 Longer-term diabatic ascent of the Nabro plume in the Asian anticyclone and estimates of radiative forcing

4.1 Diabatic ascent of the Nabro plume

Here we consider the longer-term vertical transport of the Nabro plume. CALIPSO observations show an increase in θ for the bulk of Nabro aerosol in the vicinity of the Asian anticyclone in the months following the eruption. Figure 7 shows latitude cross sections of mean cloud-cleared SR for 30–130° E for 16–30 June, 16–31 August, and 16–31 October 2011. Isopleths of mean θ are also shown. The figure shows the bulk of the Nabro aerosol above 380 K in the last 2 weeks of June. By the end of August, the bulk is found between 390 and 440 K, and by end October, it is found from 400 to 460 K. Apparent loss of material below 380 K between the end June and the end August suggests scavenging of the aerosol via cloud processes (CALIPSO shows clouds extending to 380 K in Southeast Asia; Figs. 4 and 5) and/or dilution with cleaner air in the troposphere (Vernier et al., 2011c). Slow diabatic ascent of unscavenged aerosol from the upper troposphere may also contribute (Bannister et al., 2004). Also shown in Fig. 7 are time series showing the ascent of the peak of observed SR for selected latitude bands. The data show the plume rising by 10 K month^{-1} ($\sim$ 0.3 K day^{-1}) until end of August, with a slower ascent of $\sim$ 3–5 K month^{-1} thereafter. The actual rate of diabatic lofting may be higher due to the effects of aerosol sedimentation. Nevertheless, the CALIPSO observations illustrate enhanced ascent in the lower stratosphere for air circulating the summer Asian monsoon anticyclone (Bannister et al., 2004), followed by reduced ascent later in the monsoon's dissolution.

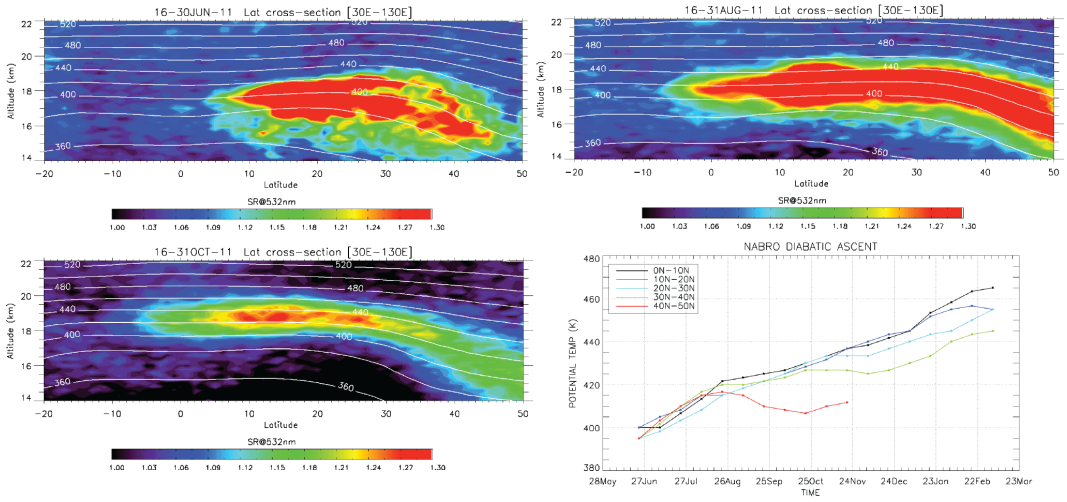

Figure 7. Latitude–altitude cross sections of mean cloud-cleared CALIPSO SR between 30 and 130° E for 16–30 June, 16–31 August, and 16–31 October, 2011. Isopleths of mean θ are also shown. Bottom-right panel: time series of θ corresponding to the peak in SR, June 2011–February 2012, for selected latitude bands (labeled).

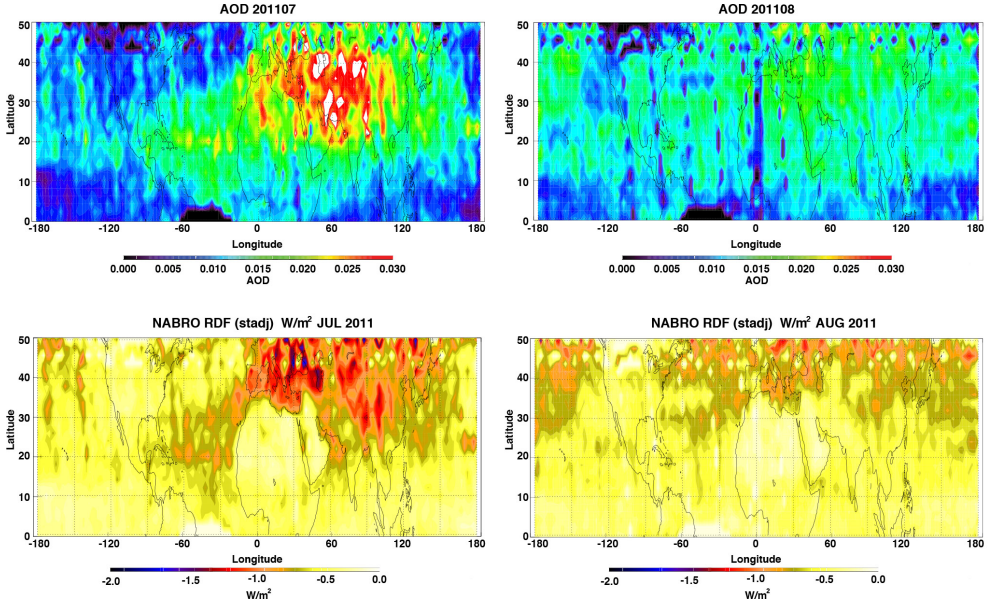

Figure 8. 532 nm AOD and TOA estimates of radiative forcing, based on monthly accumulations of CALIPSO aerosol data between 14 and 40 km altitudes for July and August, 2011. Stratospheric temperature adjustment is included in the radiative forcing calculations.

4.2 Radiative forcing estimates

We obtained estimates of the aerosol extinction from cloud-cleared CALIPSO aerosol backscatter measurements, assuming a lidar ratio of 50 sr, as before. We then used the NASA Langley Fu-Liou radiative transfer code (described earlier) to compute differences between the TOA clear-sky net radiative fluxes with and without the aerosols to estimate the net RF due to Mt. Nabro. We use an iterative method that allows the stratospheric temperature to adjust to the aerosol loading. Figure 8 shows 532 nm aerosol optical depth (AOD) and TOA estimates of radiative forcing, based on monthly accumulations of CALIPSO aerosol data between 14 and 40 km altitudes. Peak values of AOD $\sim$ 0.04–0.06 are found in July associated with the Asian anticyclone. This reflects the complete conversion of SO_2 to sulfate by end of June (Clarisse et al., 2012), followed by potential growth of aerosol particles. Figure 8 also illustrates the transport of Nabro aerosol across the tropical Atlantic in July (Bourassa et al., 2012; Sawamura et al., 2012), as part of the dispersion of aerosol throughout the Northern Hemisphere, which resulted in reduced AOD in August. Maps

of TOA radiative forcing closely follow the distributions of AOD, except over the desert regions of North Africa and Arabia, where the Nabro aerosol provides little enhancement in reflectivity over the bright underlying surfaces. Peak values of $\sim -1.6\,\mathrm{W\,m^{-2}}$ are found locally over Asia and Europe during July. For 50° S–50° N, we find monthly TOA clear-sky RF from stratospheric aerosol of −0.20 (June), −0.27 (July), −0.26 (August), and $-0.25\,\mathrm{W\,m^{-2}}$ (September), respectively. (Our TOA RF estimates respond approximately linearly to changes in assumed aerosol lidar ratio). These RF estimates are modestly (up to ∼ 0.07) larger in magnitude than the $-0.2\,\mathrm{W\,m^{-2}}$ RF estimated by Solomon et al. (2011) from CALIPSO and GOMOS (Global Ozone Monitoring by Occultation of Stars) data for the years immediately prior to the Nabro eruption, but they are small (5–10 %) compared with estimates made following the eruption of Mt. Pinatubo in 1991: $\sim -15\,\mathrm{W\,m^{-2}}$ locally, and $-4.5\,\mathrm{W\,m^{-2}}$ on average (40° S–40° N) (Minnis et al., 1993). Moreover, it is challenging to detect a TOA radiative signal due to Nabro aerosol within the background of variability as measured by the Clouds and Earth Radiant Energy System (CERES) instrument. We used the CERES data analysis tool (http://ceres-tool.larc.nasa.gov) to construct both monthly anomaly maps (not shown) and a deseasonalized time series of clear sky TOA SW (shortwave) radiative flux anomalies between 50° S and 50° N (Fig. S2 in the Supplement). Neither showed a clear SW response to the presence of Nabro aerosol. We found the standard deviation of the monthly outgoing SW time series to be $\sim 0.2\,\mathrm{W\,m^{-2}}$, similar in magnitude to the TOA RF estimates for stratospheric aerosol noted above. Positive SW anomalies are shown from mid-2011 to mid-2012 (Supplement Fig. S2), but the increase precedes rather than coincides with the Nabro eruption.

5 Conclusions

We use CALIPSO, ground-based lidar observations, and a Lagrangian trajectory model to study the emergence of volcanic aerosol layers in the low stratosphere, following the eruption of Mt. Nabro in June 2011. We find that kinematic trajectory calculations provide a qualitatively good reproduction of the timing and vertical distribution of volcanic aerosol observed 1–2 days downstream of the volcano. Further, we find that much of the aerosol layering observed by CALIPSO in the lower stratosphere over South and Southeast Asia within 10 days of the eruption can be explained by direct injection above 380 K, and quasi-isentropic differential advection in vertically sheared flow. We use Meteosat-7 brightness temperatures to identify two prominent mesoscale convective systems that likely coincide with tropospheric parts of the Nabro plume. However, our analysis indicates that these MCSs are unlikely sources of the stratospheric aerosol layers seen by CALIPSO in the latter half of June. Thus, our study does not support a critical role for deep convection in the Asian monsoon in transporting volcanic sulfate directly to the stratosphere. Nevertheless, the Asian anticyclone remains a dominant feature governing the dispersion of the Nabro plume until its dissipation in September. CALIPSO observations show the plume ascended by $\sim 10\,\mathrm{K\,month^{-1}}$ in the lower stratosphere in the anticyclone for the first 2 months following the eruption, and by ~ 3–$5\,\mathrm{K\,month^{-1}}$ thereafter. Apparent loss of aerosol below 380 K between the end of June and August suggests scavenging by cloud processes, and/or mixing with cleaner air, but slow diabatic ascent of Nabro aerosol that remains unscavenged above the level of zero diabatic heating (∼ 15 km) cannot be discounted. We also estimate top-of-the-atmosphere radiative forcing from the Nabro plume, finding it small compared with historically large eruptions, e.g., Mt. Pinatubo, and comparable to the month–month variability in outgoing SW radiative flux, as measured by CERES.

Detection of the Asian tropopause aerosol layer (ATAL) (Vernier et al., 2011b, 2014) indicates that deep convection, which transports insoluble gas-phase boundary layer pollutants to the UTLS during the East Asian monsoon, could similarly loft aerosols and their precursor gases, albeit with significant losses due to wet scavenging. Further lofting above the level of zero diabatic heating may contribute to stratospheric sulfate on timescales of months. While it seems plausible that components of the Nabro plume injected directly into the upper troposphere may have contributed to stratospheric sulfate in the following months, our study points to a simpler explanation for the rapid emergence of stratospheric aerosol layers from the Nabro eruption in South and Southeast Asia: direct injection above 380 K, followed by quasi-isentropic differential advection in vertically sheared flow.

The Supplement related to this article is available online at doi:10.5194/acp-14-7045-2014-supplement.

Acknowledgements. The authors would like to thank the SAGE II, CALIPSO, and CERES instrument teams for their support, notably M. Vaughan, Z. Liu, L. Thomason, C. Trepte, P. Taylor, S. Kato, and N. Baker. We thank B. Pierce, M. von Hobe, and D. Jacob for very helpful suggestions on the manuscript, M. Mills, B. Randel, M. Fromm, and G. Nedoluha for useful discussions. We thank A. Karnieli, and E. J. Welton for providing us with data from the MPLNET lidar at Sede Boker. We thank M. Rienecker and the NASA GMAO for providing the GEOS-5 analyses. This work was also supported by the SAGE II and CALIPSO projects and by the Atmospheric Composition Modeling and Analysis (ACMAP) Program under NASA's Science Mission Directorate.

Edited by: F. Fierli

References

Bannister, R. N., O'Neill, A., Gregory, A. R., and Nissen, K. M.: The role of the south-east Asian monsoon and other seasonal features in creating the 'tape-recorder' signal in the Unified Model, Q. J. Roy. Meteor. Soc., 130, 1531–1554. 2004,

Bluth, G. J. S., Doiron, S. D., Krueger, A. J., Walter, L. S., and Schnetzler, C. C.,: Global tracking of the SO_2 clouds from the June 1991 Mount Pinatubo eruptions, Geophys. Res. Lett., 19, 151–154, 1992.

Bourassa, A. E., Robock, A., Randel, W. J., Deshler, T., Rieger, L. A., Lloyd, N. D., Llewellyn, E. J., and Degenstein, D. A.: Large Volcanic Aerosol Load in the Stratosphere Linked to Asian Monsoon Transport, 2012, Science, 337, 78–81, 2012.

Bourassa, A. E., Robock, A., Randel, W. J., Deshler, T., Rieger, L. A., Lloyd, N. D., Llewellyn, E. J., and Degenstein, D. A.: Response to comments on "Large volcanic aerosol load in the stratosphere linked to the Asian monsoon transport", Science, 339, 6120, doi:10.1126/science.1227961, 2013.

Carn, S. A., Strow, L. L., de Souza-Machado, S., Edmonds, Y., and Hannon, S.: "Quantifying tropospheric volcanic emissions with AIRS: The 2002 eruption of Mt. Etna (Italy)," Geophys. Res. Lett., 32, L02301, doi:10.1029/2004GL021034, 2005.

Clarisse, L., Hurtmans, D., Clerbaux, C., Hadji-Lazaro, J., Ngadi, Y., and Coheur, P.-F.: Retrieval of sulphur dioxide from the infrared atmospheric sounding interferometer (IASI), Atmos. Meas. Tech., 5, 581–594, doi:10.5194/amt-5-581-2012, 2012.

Fairlie, T. D., Szykman, J., Gilliland, A., Pierce, R. B., Kittaka, C., Weber, S., Engel-Cox, J., Rogers, R. R., Tikvart, J., Scheffe, R., and Dimmick, F.: Lagrangian sampling of 3-D air quality model results for regional transport contributions to sulfate aerosol concentrations at Baltimore, MD, in summer 2004, Atmos. Environ., 43, 3275–3288, 2009.

Fromm, M., Nedoluha, G., and Charvát, Z.: Comment on "Large Volcanic Aerosol Load in the Stratosphere Linked to Asian Monsoon Transport", Science 339, 6120, doi:10.1126/science.1228605, 2013.

Fueglistaler, S., Dessler, A. E., Dunkerton, T. J., Folkins, I., Fu, Q., and Mote, P. W.: Tropical Tropopause Layer, Rev. Geophys., 47, RG1004, doi:10.1029/2008RG000267, 2009.

Guo, S., Bluth, G. J. S., Rose, W. I., and Watson, I. M.: Re-evaluation of SO_2 release of the 15 June 1991 Pinatubo eruption using ultraviolet and infrared satellite sensors, Geochem. Geophy. Geosy., 5, Q04001, doi:10.1029/2003GC000654, doi:10.1029/2003GC000654, 2004.

Holton, J. R., Haynes, P. H., McIntyre, M. E., Douglass, A. R., Rood, R. B., and Pfister, L.: Stratosphere-troposphere exchange, Rev. Geophys., 33, 403–439, doi:10.1029/95RG02097, 1995.

Krotkov, N., Yang, K., and Carn, S.: A-Train observations of Nabro (Eritrea) eruption on June 13–16 2011, http://aura.gsfc.nasa.gov/science/feature-20120305b.html (last access: 3 July 2014), 2011.

McCormick, M. P., Thomason, L. W., and Trepte, C. R.: Atmospheric Effects of the Mt. Pinatubo Eruption, Nature, 373, 399–404, 1995.

Minnis, P., Harrison, E. F., Stowe, L. L., Gibson, G. G., Denn, F. M., Doelling, D. R., and Smith Jr., W. L.: Radiative climate forcing by the Mount Pinatubo eruption, Science, 259, 1411–1415, 1993.

Müller, D., Ansmann, A., Mattis, I., Tesche, M., Wandinger, U., Althausen, D., and Pisani, G.: Aerosol-type-dependent lidar ratios observed with Raman lidar, J. Geophys. Res., 112, D16202, doi:10.1029/2006JD008292, 2007.

Natarajan, M., Pierce, R. B., Schaack, T. K., Lenzen, A. J., Al-Saadi, J. A., Soja, A. J., Charlock, T. P., Rose, F. G., Winker, D. M., and Worden, J. R.: Radiative forcing due to enhancements in tropospheric ozone and carbonaceous aerosols caused by Asian fires during spring 2008, J. Geophys. Res., 117, D06307, doi:10.1029/2011JD016584, 2012.

Neely III, R. R., Toon, O. B., Solomon, S., Vernier, J.-P., Alvarez, C., English, J. M., Rosenlof, K. H., Mills, M. J., Bardeen, C. G., Daniel, J. S., and Thayer, J. P.: Recent anthropogenic increases in SO_2 from Asia have minimal impact on stratospheric aerosol, Geophys. Res. Lett., 40, 999–1004, doi:10.1002/grl.50263, 2013.

Pierce, R. B. and Fairlie, T. D. A.: "Chaotic advection in the stratosphere: Implications for the dispersal of chemically perturbed air from the polar vortex", J. Geophys. Res., 98, 18,589–18,595, 1993.

Pierce, R. B., Grose, W. L., Russell III, J. M., and Tuck, A. F.: Evolution of southern hemisphere spring air masses observed by HALOE, Geophys. Res. Lett., 21, 213–216, 1994.

Pierce, R. B., Fairlie, T. D., Remsberg, E. E., Russell III, J. M., and Grose, W. L.: HALOE Observations of the Arctic Vortex during the 1997 Spring: Horizontal Structure in the Lower Stratosphere, Geophys. Res. Lett., 24, 2701–2704, 1997.

Portmann, R. W., Solomon, S., Garcia, R. R., Thomason, L. W., Poole, L. R., and McCormick, M. P.: Role of aerosol variations variations in anthropogenic ozone depletion in polar regions, J. Geophys. Res., 101, 22,991–23,006, 1996.

Randel, W. J. and Jensen, E. J.: Physical processes in the tropical tropopause layer and their roles in changing climate, Nat. Geosci., 6, 169–176, 2013.

Rienecker, M. M., Suarez, M. J., Todling, R., Bacmeister, J., Takacs, L., Liu, H.-C., Gu, W., Sienkiewicz, M., Koster, R. D., Gelaro, R., Stajner, I., and Nielsen, J. E.: The GEOS-5 Data Assimilation System–Documentation of Versions 5.0.1, 5.1.0, and 5.2.0, NASA/TM–2008–104606, Vol. 27, Technical Report Series on Global Modeling and Data Assimilation, Volume 27, edited by: Suarez, M. J., 2008.

Robock, A.: Volcanic eruptions and climate, Rev. Geophys., 38, 191–219, doi:10.1029/1998RG000054, 2000.

Rodriguez, J. M., Ko, M. K. W., and Sze, N. D.: Role of heterogeneous conversion of N_2O_5 on sulphate aerosols in global ozone losses, Nature, 352, 134–137, 1991.

Rose, F., Charlock, T. P., Fu, Q., Kato, S., Rutan, D., and Jin, Z.: CERES Proto-Edition 3 radiative transfer: Model tests and radiative closure over surface validation sites, Proceedings of 12 th Conference on Atmospheric Radiation (AMS), Madison, Wisconsin, 2006.

Sawamura, P., Vernier, J.-P., Barnes, J. E., Berkoff, T. A., Welton, E. J., Alados-Arboledas, L., Navas-Guzmán, F., Pappalardo, G., Mona, L., Madonna, F., Lange, D., Sicard, M., Godin-Beekmann, S., Payen, G., Wang, Z., Hu, S., Tripathi, S. N., Cordoba-Jabonero, C., and Hoff, R. M.: Stratospheric AOD after the 2011 eruption of Nabro volcano measured by lidars over the Northern Hemisphere, Environ. Res. Lett. 7, 034013, doi:10.1088/1748-9326/7/3/034013, 2012.

Schoeberl, M. R.: Extratropical stratosphere-troposphere mass exchange, J. Geophys. Res. 109, D13303, doi:10.1029/2004JD004525, 2004.

Solomon, S., Sanders, R. W., Garcia, R. R., and Keys, J. G.: Increased chlorine dioxide over Antarctica caused by volcanic aerosols from Mount Pinatubo, Nature, 363, 245–248, 1993.

Solomon, S., Daniel, J. S., Neely III, R. R., Vernier, J. P., Dutton, E. G., and Thomason, L. W.: The Persistently Variable "Background" Stratospheric Aerosol Layer and Global Climate Change, Science, 333, 866–870, doi:10.1126/science.1206027, doi:10.1126/science.1206027, 2011.

Vernier, J.-P., Pommereau, J. P., Garnier, A., Pelon, J., Larsen, N., Nielsen, J., Christensen, T., Cairo, F., Thomason, L. W., Leblanc, T., and McDermid, I. S.: Tropical stratospheric aerosol layer from CALIPSO lidar observations, J. Geophys. Res., 114, D00H10, doi:10.1029/2009JD011946, 2009.

Vernier, J.-P., Thomason, L. W., Pommereau, J.-P., Bourassa, A., Pelon, J., Garnier, A., Hauchecorne, A., Blanot, L., Trepte, C., Degenstein, D., and Vargas, F.: Major influence of tropical volcanic eruptions on the stratospheric aerosol layer during the last decade, Geophys. Res. Lett., 38, L12807, doi:10.1029/2011GL047563, 2011a.

Vernier, J.-P., Thomason, L. W., and Kar, J.: CALIPSO detection of an Asian tropopause aerosol layer, Geophys. Res. Lett., 38, L07804, doi:10.1029/2010GL046614, 2011b.

Vernier, J.-P., Pommereau, J.-P., Thomason, L. W., Pelon, J., Garnier, A., Deshler, T., Jumelet, J., and Nielsen, J. K.: Overshooting of clean tropospheric air in the tropical lower stratosphere as seen by the CALIPSO lidar, Atmos. Chem. Phys., 11, 9683–9696, doi:10.5194/acp-11-9683-2011, 2011c.

Vernier, J.-P., Thomason, L. W., Fairlie, T. D., Minnis, P., Palikonda, R., and Bedka, K. M.: Comment on "Large Volcanic Aerosol Load in the Stratosphere Linked to Asian Monsoon Transport", Science, 339, 6120, doi:10.1126/science.1227817, 2013a.

Vernier, J.-P., Fairlie, T. D., Murray, J. J., Tupper, A., Trepte, C., Winker, D., Pelon, J., Garnier, A., Jumelet, J., Pavolonis, M., Omar, A. H., and Powell, K. A.: An advanced system to monitor the 3D structure of diffuse volcanic ash clouds, J. Appl. Meteorol. Clim., 52, 2125—2138, doi:10.1175/JAMC-D-12-0279.1, 2013b.

Vernier, J.-P., Fairlie, T. D., Thomason, L. W., Natarajan, M., Wienhold, F. G., Bian, J., and Martinsson, B. G.: Increase in Upper Tropospheric Aerosol Levels and its potential connection with Asian Pollution , J. Geophys. Res.-Atmos., submitted, 2014.

Winker, D. M., Pelon, J., Coakley Jr., J. A., Ackerman, S. A., Charlson, R. J., Colarco, P. R., Flamant, P., Fu, Q., Hoff, R., Kittaka, C.,Kubar, T. L., LeTreut, H., McCormick, M. P., Megie, G., Poole, L., Powell, K.,Trepte, C., Vaughan, M. A., and Wielicki, B. A.: The CALIPSO mission: A global 3D view of aerosols and clouds, B. Am. Meteorol. Soc., 91, 1211–1229, doi:10.1175/2010BAMS3009.1, 2010.